JOURNAL OF AIRCRAFT
Vol. 45, No. 2, March–April 2008

Relaxed-Wake Vortex-Lattice Method Using Distributed Vorticity Elements

Götz Bramesfeld* and Mark D. Maughmer†
Pennsylvania State University, University Park, Pennsylvania 16802

DOI: 10.2514/1.31665

A lifting-surface method is presented that uses elements having distributed vorticity to model lifting surfaces and their shed wakes. Using such distributed vorticity elements allows the representation of a force-free continuous wake-vortex sheet that is free of numerical singularities and is thus robust in its numerical rollup behavior. Unlike other potential-flow methods that use discrete vortex filaments having solid-core models at their centers to avoid problems with the singularities, the numerical robustness of the new method is achieved without the subsequent solution being dependent on the choice of a cutoff distance or core size. The computed loads compare well with results of classical theory and other potential-flow methods. Its numerical robustness, computational speed, and ability to predict loads accurately make the new method ideal for the investigation of applications in which the loadings on a lifting surface depend strongly on the influence of the wake and its shape, as is the case for the two application examples presented: formation flight and rotating-wing systems.

Nomenclature

A, B, C	=	circulation coefficients
b	=	wingspan
C_{Di}	=	induced-drag coefficient
C_L	=	lift coefficient
c	=	wing chord
c_l	=	section-lift coefficient
c_r	=	root chord
e	=	span efficiency
k	=	positive constant
M_∞	=	freestream Mach number
m	=	number of elements along the chord
n	=	number of elements along the half-span
V_∞	=	freestream velocity
w_2	=	velocity induced by a vortex sheet with a linear vorticity distribution in the spanwise direction
x, y, z	=	local reference frame
x_t	=	wingtip location
α	=	angle of attack
Γ	=	circulation
γ	=	vorticity
Δx	=	streamwise spacing between fuselage centerlines
Δx_{wake}	=	streamwise step size in the wake
Δy	=	lateral spacing between fuselage centerlines
η_i	=	distributed vorticity element half-span
ξ, η, ζ	=	local reference frame of the distributed vorticity element
φ	=	sweep angle of the distributed vorticity element

Subscripts

l.e.	=	values computed along the leading edge
t.e.	=	values computed along the trailing edge
Trefftz	=	values computed in the Trefftz plane

Received 17 April 2007; revision received 14 November 2007; accepted for publication 16 November 2007.

*Visiting Assistant Professor, Department of Aerospace Engineering; currently Assistant Professor, Department of Aerospace and Mechanical Engineering, Saint Louis University, St. Louis, MO. Member AIAA.

†Professor, Department of Aerospace Engineering. Associate Fellow AIAA.

Introduction

GENERALLY, potential-flow methods use discrete vortex filaments to account for the vorticity in the shed wake. The linearity of their governing equations makes them ideal for numerical applications because of their computational speed and ability to predict loads accurately. The singularity at the center of the discrete vortex filament, however, results in several numerical challenges: for example, when a wake filament of an upstream wing contacts or passes in close proximity to a control point of a downstream wing. The resulting induced velocities can be extremely large, altering the flowfield at the control point considerably, and thus have an unrealistic influence on the local circulation. One way to avoid this problem is simply to prescribe the location of the surface and wake elements in a fashion that prevents any close encounters. This is difficult, however, for the cases when the wake is not assumed to be rigid and is instead allowed to roll up.

The representation of a force-free wake does capture the effects that are due to wake rollup. These effects can be significant when a strong interaction exists between lifting surfaces and their wakes. Such interactions are found, for example, with formation flight or rotating-wing systems. In the former case, the loads of the second aircraft depend on the amount of rollup that the lead-aircraft wake has experienced up to that point. In the case of a rotating-wing system (for example, a helicopter rotor in hover), the loads of each blade are strongly influenced by the velocities induced by the wake that is shed by either a preceding blade or by that particular blade during the previous rotation.

In considering a relaxed wake, numerical issues can arise in the wake during the numerical relaxation process. As the trailing filaments are displaced with the local flowfield, the contribution of two filaments can become quite large if the filaments intersect or come in close proximity during one time step. As a consequence of the infinite velocities at the center of the singularity, irrationally large displacements occur and the wake becomes erratic. This behavior is exacerbated with a higher density of wake filaments, longer time steps for the numerical wake relaxation, and wake models that extend far downstream of the trailing edge. The latter is a particular issue when modeling the wakes of rotary wings, in that an accurate representation requires the wake to be tracked for several rotations.

Although the viscous-core model eliminates numerical issues related to the singularity at the center of a filament, the choice of core size can have a significant influence on the solution. Furthermore, the solid core does not resolve issues such as vortex pairing or the intersecting of two filaments in the wake.

A representation using a continuous vortex sheet avoids many of the singularity issues that accompany discrete vortex filaments. The

velocities that such a sheet induces are finite everywhere except in the plane of the sheet, in which the tangential velocity is undefined but numerically taken to be zero. Early analytical studies examined the rollup behavior of a zero-thickness vortex sheet in the Trefftz plane, which originated from an elliptical spanwise circulation distribution [1]. In [2], it is demonstrated that an infinitely thin free-wake sheet is numerically feasible with the help of smoothing parameters. The numerical solution, however, appears to be more robust when thickness is introduced to the wake-vortex sheet [3,4]. Although numerically feasible, either approach has limitations that are very similar to those of the solid-core approach.

The numerical implementation of the discretization of a continuous vortex sheet using elements with distributed vorticity encounters its own set of difficulties. Along the edges of each fundamental element [5], the velocity contribution to that element is singular. Although the overall solution remains finite, because the singular contributions of two neighboring elements cancel each other, the numerical management of an individual edge is difficult. Even the use of smoothing functions for the extreme velocities is of limited value because, as with the solid-core approach, the solution becomes dependent on the smoothing function used [6].

The approach introduced here allows a simple numerical application of a discretized model of a continuous vortex sheet that treats the singularities along the edges of each elementary vortex sheet without smoothing functions or other numerical corrections that alter the velocities induced by the potential-flow model. The subsequent induced velocities of the discretized wake are finite, avoiding most of the singularity issues that result when vortex filaments are used to model the wake. The resulting method allows for the accurate representation of a force-free wake that captures wake-rollup behavior well and is more numerically robust than many previous approaches.

Distributed Vorticity Element

In the study presented herein, the flowfield is modeled using a potential-flow method that relies on distributed vorticity elements. A more comprehensive discussion of the method can be found in [7]. As shown in Fig. 1, a distributed vorticity element has vortex filaments along its leading and trailing edges. These two filaments have spanwise circulation distributions that are parabolic and of opposite orientations. A vortex sheet with a linearly varying vorticity distribution maintains the total vorticity in the streamwise direction between the two filaments. The vorticity of the sheet is aligned along the local flow direction (that is, along the ξ axis). The sheet lies in the ξ–η plane, and thus the ζ axis is normal to the plane of the vortex sheet of the distributed vorticity element.

The velocity that is induced by a distributed vorticity element can be computed by adding the analytical solutions of two sets of a vortex filament and a semi-infinite vortex sheet, as shown in Fig. 1 [7]. One set begins at the leading edge of the distributed vorticity element. The second set, for which the circulation and vorticity distributions are of opposite orientations, begins at the trailing edge of the element. Downstream of the trailing edge of the element, the influence of the two vortex sheets is effectively canceled out.

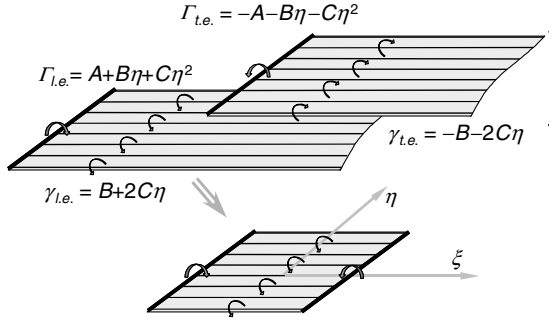

Fig. 1 A distributed vorticity element is composed of vortex filaments along its leading and trailing edges and of two semi-infinite vortex sheets.

The lifting-surface method with a force-free-wake model presented herein is based on the multiple-lifting-line method of [8]. The velocities that a vortex filament segment induces with its parabolic circulation distribution at an arbitrary point $P_0(\xi_0, \eta_0, \zeta_0)$ require the integration over the elementary wingspan from $-\eta_i$ to η_i:

$$\underline{w}_1(\xi_0, \eta_0, \zeta_0) = \int_{-\eta_i}^{\eta_i} \frac{A + \eta B + \eta^2 C}{4\pi r_1^3} \begin{bmatrix} -\zeta_0 \\ \zeta_0 \tan\phi \\ \xi_0 - \eta_0 \tan\phi \end{bmatrix} \mathrm{d}\eta \qquad (1)$$

A similar integration yields the velocity induced by the semi-infinite vortex sheet:

$$\underline{w}_2(\xi_0, \eta_0, \zeta_0) = \int_{-\eta_i}^{\eta_i} \frac{B + 2\eta C}{4\pi((\eta_0 - \eta)^2 + \zeta_0^2)} \left(\frac{\xi_0 - \eta \tan\varphi}{r_1} + 1 \right) \begin{bmatrix} 0 \\ -\zeta_0 \\ \eta_0 - \eta \end{bmatrix} \mathrm{d}\eta \qquad (2)$$

where

$$r_1 = \sqrt{(\xi_0 - \eta \tan\varphi)^2 + (\eta_0 - \eta)^2 + \zeta_0^2}$$

ξ, η, and ζ are the coordinates in the local reference frame of the basic element and φ is its leading-edge sweep angle, as indicated in Fig. 2.

The integrands in Eqs. (1) and (2) exhibit several singularities. In addition to the singularity at the centers of the vortex filaments, further singularities are associated with the vortex sheet and are the subject of the following discussion.

Semi-Infinite Vortex Sheet

As is apparent in Eq. (2), the vortex sheet induces two velocity components: one that is tangential to the plane of the sheet in the spanwise η direction and one that is normal to the plane of the sheet. Except in the plane of the sheet, in which it is undefined, the tangentially induced-velocity component is finite everywhere. In the plane of the sheet itself, the tangential velocity is set to zero for numerical purposes. The velocities induced by the vortex sheet normal to its plane are finite except along the edges of the sheet, where they can be singular. For example, the velocity induced along the leading edge of the semi-infinite vortex sheet becomes singular if the leading edge is swept. Without sweep, the self-induced velocity along the leading edge is half the value of the doubly infinite vortex sheet. Further singularities are present along the side edges of the sheet if the vorticity is nonzero there. These singularities complicate the numerical implementation of a discretized model.

Discretizing a Continuous Vortex Sheet

A continuous spanwise vorticity distribution is shown in Fig. 3 for a vortex sheet having a triangular distribution of strength, going to zero at $\eta = -1$ and 4.2. The subsequent induced normal velocity $w_{2\text{total}}$ is finite everywhere in the plane of the sheet. When discretizing this sheet and its triangular vorticity distribution with

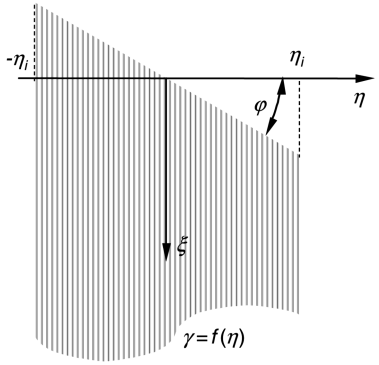

Fig. 2 The semi-infinite vortex sheet of [8].

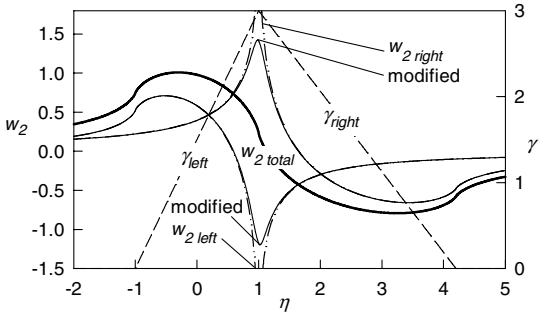

Fig. 3 A spanwise distribution of the normal velocity that is induced in the plane of two semi-infinite vortex sheets. The left sheet spans from $\eta = -1$ to 1 and the right sheet spans from $\eta = 1$ to 4.2. The dashed line denotes the spanwise vorticity distributions and the solid line denotes the total induced velocity.

two separate sheets having linear vorticity distributions γ_{left} and γ_{right}, the overall induced velocity should clearly remain unchanged. The individual velocity contributions of each discrete vortex-sheet element, $w_{2\text{left}}$ and $w_{2\text{right}}$, depend in part on logarithmic terms of the following form:

$$w_2(\eta) \sim \ell_n\left[\frac{(\eta - \eta_i)^2}{(\eta + \eta_i)^2}\right] \tag{3}$$

where η is the local span coordinate of the point at which the induced velocity is being computed, and η_i is the half-span of the semi-infinite vortex sheet element. As the common boundary of the two neighboring elements is approached at $\eta = 1$, the numerator of the logarithmic expression of one of the vortex-sheet elements becomes zero; simultaneously, the denominator of the other element approaches zero at the same rate. If the vorticities at the common border are of equal strengths, the subsequent velocity singularities of $w_{2\text{left}}$ and $w_{2\text{right}}$ are of the same magnitude but of opposite sign and thus cancel one another. Consequently, the overall induced velocity $w_{2\text{total}}$ remains finite and unchanged to the original case of the vortex sheet with continuous triangular vorticity distribution.

Treatment of the Side-Edge Singularities

To be able to numerically handle the discretized representation of a continuous vortex sheet without altering the overall induced-velocity field, the logarithmic term in Eq. (3) requires further treatment. By adding additional singularities to the side edges of each individual vortex-sheet element, the original singularities are canceled and each element becomes numerically well-behaved, as indicated by the modified induced velocities in Fig. 3. Also, as the added singularities of two neighboring elements cancel one another, the combined induced velocity remains unaffected. The additional singularities to each side edge of a vortex-sheet element modify the numerator and denominator of the logarithmic term of Eq. (3) with the sum of a positive constant k, such that

$$w_2(\eta) \sim \ell_n\left[\frac{k + (\eta - \eta_i)^2}{k + (\eta + \eta_i)^2}\right] \tag{4}$$

The rate at which the influence of the additional singularity diminishes with increasing distance to its location depends on the size of the constant k. A smaller k reduces the impact on the corresponding induced flow component further away, but increases its peak at the edge itself. Independently of this, the combined velocity $w_{2\text{total}}$ will remain unchanged if the same constant k is used for two neighboring vortex-sheet elements.

Treatment of the Leading-Edge Singularities

As mentioned before, the velocity that is induced normal to the plane of a vortex sheet is singular along its leading edge if the leading edge is swept. Without sweep, however, the induced velocity is half the value of a doubly infinite vortex sheet. To illustrate this, the

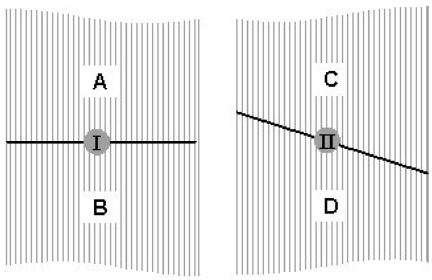

Fig. 4 Modeling a vortex sheet that is continuous along the direction of its vorticity orientation using two semi-infinite vortex sheets.

sketch on the left of Fig. 4 depicts a doubly infinite vortex sheet. This sheet can also be represented with two semi-infinite vortex sheets (A and B) that join along the solid line. Clearly, in this case, each semi-infinite vortex sheet contributes half of the total induced velocity. On the right side of Fig. 4, the same doubly infinite vortex is modeled using two semi-infinite vortex sheets for which the common boundary is swept. Although the total normal induced velocity at point II is the same as at point I, it can be shown that the individual contributions of the semi-infinite vortex sheets C and D are singular at point II, due to the swept edges of the sheets [7]. Similar to the side-edge singularities of Eq. (3), these singularities are logarithmic in nature and cancel at the joined edge of both sheets C and D, thus resulting in the finite total velocity.

Because the singularity along a swept leading edge of a vortex sheet is similar in nature to those found along the sides of a discontinuous sheet, a similar treatment is possible; that is, an additional singularity can be introduced to cancel the original one. The mathematical approach is similar to that given by Eq. (4), with the addition of a positive constant to the numerator and denominator of the logarithmic expression. Subsequently, when describing a doubly infinite vortex sheet using semi-infinite vortex sheets, the total induced velocity remains unchanged, although the individual velocity contributions are now finite.

Limitation of the Singularity Treatment

A limitation of the method that uses distributed vorticity elements is related to the discontinuity that occurs at the tip of the lifting surface and its subsequent wake. There, although the bound circulation approaches zero, the shed vorticity is usually nonzero. The extreme example is the elliptical circulation distribution, which has zero circulation at the tip but sheds an infinite amount of vorticity there. Clearly, this discontinuity represents a limit of modeling a flowfield using potential theory, because in a real fluid, viscous effects strongly influence that region. This limitation is independent of whether or not vortex filaments or vortex sheets are used, although the former typically entails a nonzero circulation at the wingtip.

The singular velocity along the wake edge is avoided by using the modification given in Eq. (4). In that case, however, the additional singularity at the edge of the wake-vortex sheet is unbalanced without a neighboring element. As a consequence, the additional singularity can affect the remaining flowfield. The degree of that influence greatly depends on the size of k in Eq. (4), which governs the peak size of the induced velocity at the edge of a distributed vorticity element and how fast that influence diminishes. As the value of k decreases, the velocity peak at the edge of the vortex-sheet element becomes more pronounced and its impact further away becomes more reduced. The limiting case is $k = 0$, which returns the original result of Eq. (3). The velocity peak only becomes a concern, however, when the induced normal velocity must be computed at the wake edge, primarily during the relaxation process. In [7], a k value of 1% of the half-span of the vortex-sheet element at the wake tip yielded a relatively smooth overall velocity distribution that experienced only a minor influence by the tip. This value reduces the impact on the circulation distribution to a minimum without causing significant local velocity peaks in the flowfield. The latter is helped by the fact that the locally computed flowfield is the composition of

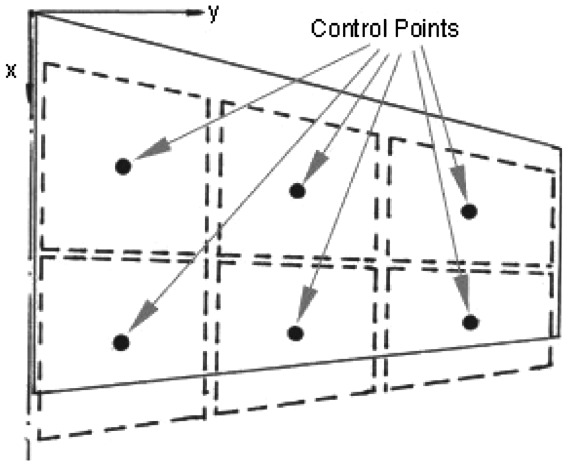

Fig. 5 Paneling of the lifting surface (solid lines) with distributed vorticity elements (dashed lines).

the influences of many vortex-sheet elements. Nevertheless, even with the singularity along the outer edge of the wake, distributed vorticity elements eliminate the singularities in the remaining flowfield that are otherwise present when using vortex filaments.

Potential-Flow Model Using Distributed Vorticity Elements

Lifting-Surface Representation

A lifting surface is represented by arranging several distributed vorticity elements across the span. The spanwise vortex filaments and their parabolic strength form second-order splines to account for the bound circulation. The vortex sheet between the leading- and trailing-edge filaments has a continuous spanwise vorticity distribution. Several such spanwise systems can be positioned at different chordwise locations, as shown in Fig. 5.

The circulation coefficients A, B, and C of each distributed vorticity element are determined by solving a system of linear equations that satisfies three boundary conditions: flow tangency at a control point and circulation and vorticity strengths that are continuous in the spanwise direction across the boundary between two distributed vorticity elements. Although it is possible to introduce thickness, in this study, the elements were distributed over the chord, or zero-lift, surface to limit the computing time. Thus, it is essentially a vortex-lattice method.

Because the elements remain planar and are, in fact, only truly continuous in the spanwise direction along their leading-edge vortex filaments, leakage may occur between the distributed vorticity elements of a lifting surface that has twist. Nevertheless, the leakage will have a negligible influence if a sufficient number of spanwise panels are used.

Development of the Wake

The wake is developed using a time-stepping method. As the wing progresses forward with each time step, a new spanwise row of distributed vorticity elements is emitted into the wake from the trailing edge. The vorticity distribution of the wake elements depends on the strength of the circulation of the surface elements that are located along the trailing edge. To reduce the computational effort and eliminate any singularities in the wake, the leading and trailing vortex filaments of the wake elements are omitted, which is permissible for steady-state conditions having constant streamwise vorticity strength.

To achieve a force-free wake, the distributed vorticity elements are displaced with the local velocity during each time step. During the relaxation process, the wake elements are allowed to roll, pitch, yaw, and stretch. As the wake elements are stretched and compressed, their vorticity distributions must be adjusted to keep the total circulation unchanged. Thus, for a distributed vorticity element,

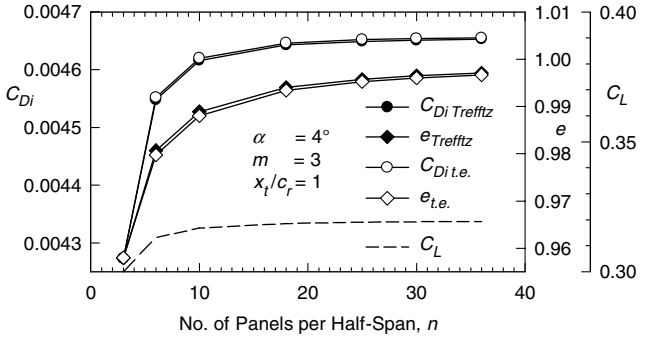

Fig. 6 Forces and span efficiencies of an elliptical wing with a straight trailing edge computed using the multiple-lifting-line method [8]. The induced drag is computed in the Trefftz plane and by applying the Kutta–Joukowsky theorem along the trailing edge of the wing.

$$\frac{1}{2\eta_i}\int_{-\eta_i}^{\eta_i}\Gamma(\eta)\mathrm{d}\eta = \text{const} \tag{5}$$

must remain constant, where η_i is the half-span of the distributed vorticity element with its spanwise circulation distribution $\Gamma(\eta)$. With steady conditions, the integral value of Eq. (5) is constant for wake elements of a particular span location, the value depending on the vorticity shed at the trailing edge of the span location of interest.

As is the case with the lifting surface, leakage can occur between the wake elements, which remain planar as they rotate and stretch during the relaxation process. This, however, only becomes an issue if the local velocities were to be computed in such a gap between two wake elements. In such a case, the velocity peaks induced by the edge of one distributed vorticity element may be unbalanced. To minimize such problems during the relaxation process, the wake elements are attached in the spanwise direction at their midchord locations and in the streamwise direction at their midspan locations. Thus, it is ensured that no gaps occur at the points at which the local induced velocities are computed during the relaxation process.

Lift and Induced Drag Determination

Lift is computed along the vortex filaments of the distributed vorticity elements of the lifting surface. The force is composed of a part due to the freestream flow and a part due to the induced velocity. The freestream force contribution uses an analytical solution to integrate the lift force across the span of each bound vortex. The lift due to the induced velocities at each surface element is determined using a numerical integration.

The induced drag is computed by taking the cross product between the circulation that is shed into the wake at the trailing edge and the velocity induced by the wake at this location [9–11]. A comparison of the computed drags of this near-field approach and of a Trefftz-plane integration is given in Fig. 6 for a wing with an elliptical chord distribution and a straight trailing edge. Both cases use the fixed-wake model of the multiple-lifting-line method of [8]. Also shown in this figure are the lift force and the subsequent span efficiencies that are based on the two different drag estimations. The two drag-calculation methods and their corresponding span efficiencies display differences of less than a tenth of a percent.

Special attention is required when determining the induced drag of a wing with a swept trailing edge, because the normal velocity induced by the wake vortex sheet is singular along its swept leading edge [8]. In spite of the singular velocity, the induced drag is finite and equal to that of a system without sweep but having an equivalent spanwise circulation distribution [12,13]. Thus, to predict the drag along a swept trailing edge, this edge is essentially deswept for the numerical computation, whereas the spanwise circulation distribution is maintained. Drag results of this approach are plotted in Fig. 7 for wings with elliptical chord distributions and varying sweep angles; $x_t/c_r = 0$ denotes a straight leading edge, $x_t/c_r = 0.25$ is a straight quarter-chord line, and $x_t/c_r = 1$ is a straight trailing edge. The forces and span efficiencies were computed using

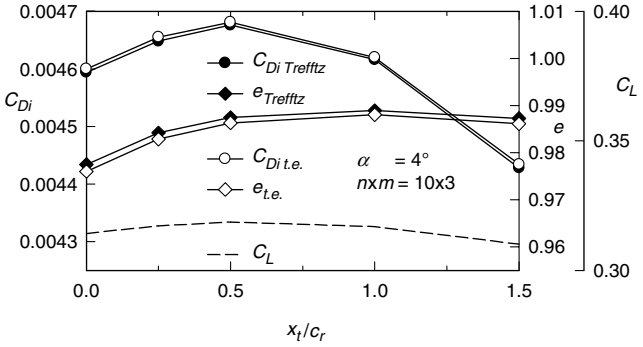

Fig. 7 Forces and span efficiencies of the multiple-lifting-line method [8] using results from the Trefftz plane and Kutta–Joukowsky along the trailing edge of a wing with an elliptical chord distribution and varying trailing-edge sweeps.

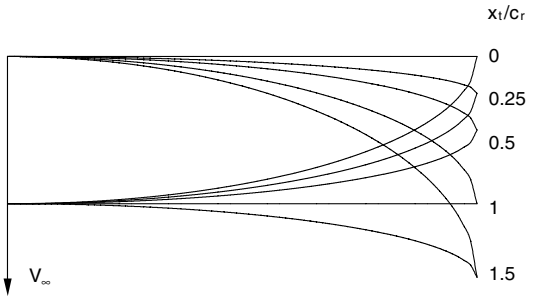

Fig. 8 Elliptical planforms with various tip locations.

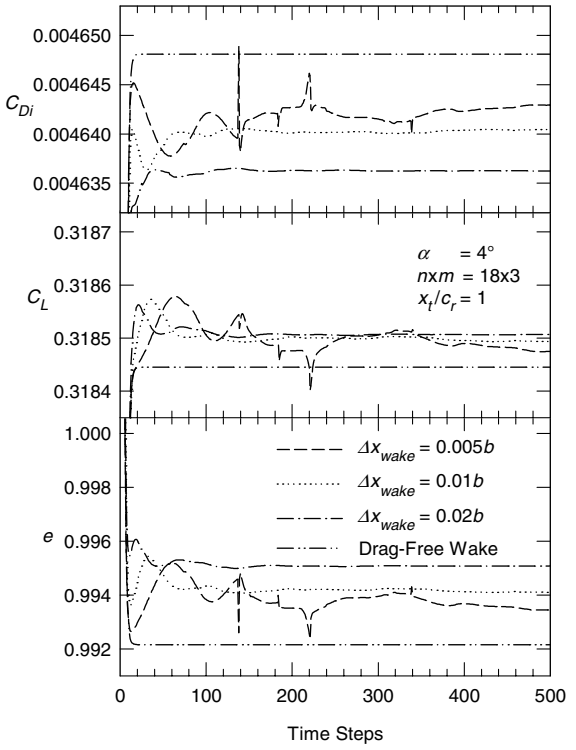

Fig. 9 Convergence behavior of drag and lift forces and the span-efficiency factor of a wing with an elliptical chord distribution and straight trailing edge using various step sizes in the relaxed wake.

the fixed-wake multiple-lifting-line method of [8]. As evident in Fig. 7, the near-field results are in good agreement with the values that were determined in the Trefftz plane, despite the varying sweeps.

The drag evaluation along the trailing edge is much more suitable for a relaxed wake than is a Trefftz-plane integration. The Trefftz-plane results require the knowledge of the exact shape of the wake shape far away from the lifting surface and is sensitive to even small errors in the shape [14]. In comparison, the drag estimation along the trailing edge is not very dependent on the accuracy in shape of an aged wake far away from the trailing edge.

Validation

To validate the method described in the previous section, the forces on wings having elliptical chord distributions were computed and compared with results obtained elsewhere [10,14,15]. The elliptical planforms considered have aspect ratios of 7 and various amounts of sweep. An angle attack of 4 deg is used, which corresponds to a cruise-lift coefficient of approximately 0.32. The distributed vorticity elements are distributed linearly along the span and the chord of the lifting surface.

The respective planforms are shown in Fig. 8, where $x_t/c_r = 0$ denotes the wing with an unswept leading edge, and $x_t/c_r = 1$ is the crescent wing that has an unswept trailing edge. Only the latter planform has a fixed drag-free wake that has a planar trace in the Trefftz plane, independent of angle of attack. In comparison, the straight wake shed from the forward-swept trailing edge of the classical elliptical wing (that is $x_t/c_r = 0.25$) has a growing dihedral with increasing angles of attack, and its subsequent trace in the Trefftz plane has an elliptical shape. Conversely, the Trefftz-plane projection of an aft-swept trailing edge has an anhedral with positive angles of attack. Thus, the elliptical planform with a straight trailing edge most closely matches the assumptions made in the classical lifting-line theory regarding a planform having an elliptical circulation distribution.

Convergence Study

The convergence behaviors of the induced-drag coefficient, lift coefficient, and span efficiency are shown in Fig. 9 for different step sizes in the wake for a wing with an elliptical chord distribution and a straight trailing edge ($x_t/c_r = 1$). The wake is developed using a time-stepping method and, consequently, the strength of the shed vorticity changes significantly in the early stage of the wake evolution. The lifting surface was modeled with $m \times n = 18 \times 3$ distributed vorticity elements across the half-span and the chord, respectively. Three different wake-step sizes were used to develop the relaxed force-free wake: 0.5, 1, and 2% of the wingspan. Also shown in the figure is the convergence behavior of the equivalent values of a fixed drag-free wake that is shed from the trailing edge of the wing along the direction of the freestream.

Overall, the computed solutions converge well and are numerically well-behaved, even after the wake has been developed for up to 10 wingspan lengths. In general, convergence is reached within approximately 60 time steps. Within the first 20 time steps, the results of all four wake-step sizes are within a half-percent of their converged value. Any oscillatory behavior is strongly damped, with the exception of occasional peaks of the relaxed wake, which uses the smallest step size of 0.5% of the wingspan. Although these outliers are most likely the result of leakage issues in the relaxed wake, it is significant to notice that they remain limited in value and are strongly damped.

Panel-Density Effects

The influence of the spanwise paneling density on lift and drag coefficients and the span efficiency is shown in Fig. 10. The linear spanwise panel distribution varies from 3 to 36 distributed vorticity elements per half-span, with three elements used along the chordwise direction of the lifting surface. The force and span-efficiency values rise asymptotically with an increasing number of spanwise panels. Although lift and drag appear to be leveling off at the higher panel density in the spanwise direction, the span-efficiency factor continues to approach the theoretical value of 1.

The variation of the element density along the chordwise direction has only a minor impact on the convergence behavior, as shown in Fig. 11. In this figure, the chordwise paneling density was increased

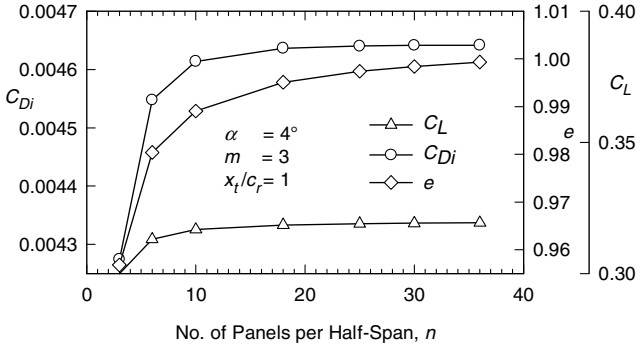

Fig. 10 Behavior of lift, drag, and span efficiency as functions of the varying density of distributed vorticity elements in the spanwise direction of a wing with an elliptical chord distribution and straight trailing edge.

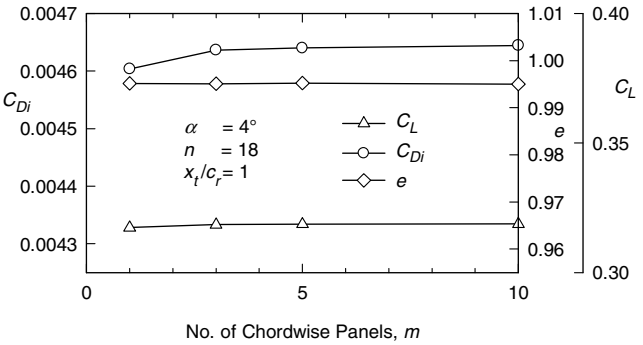

Fig. 11 Behavior of lift, drag, and span efficiency as functions of the varying density of distributed vorticity elements in the chordwise direction of a wing with an elliptical chord distribution and straight trailing edge.

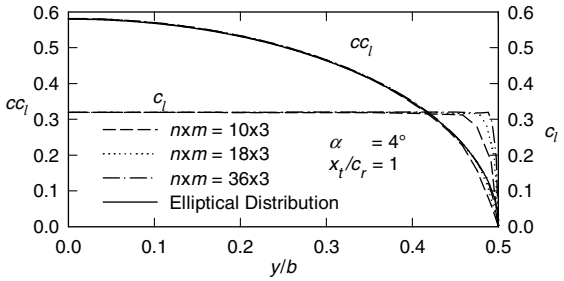

Fig. 12 Comparison of spanwise distribution of the lift and lift coefficient of an elliptical wing with aspect ratio of 7 and different panel densities.

from 1 to 10 for a wing with 18 panels across its half-span. The computed values are relatively constant for three or more elements in the chordwise direction.

Lift Distribution

The spanwise lift distribution for the case of the wing with an elliptical chord distribution and a straight trailing edge is plotted in Fig. 12. The lifting surface is modeled with 10, 18, and 36 distributed vorticity elements along the span and 3 along the chord. Also plotted in this figure is the theoretical case of an elliptical lift distribution. The differences between theory and the calculated solution are small and occur mainly in the very tip region, in which the second-order splines formed by the distributed vorticity elements fail to follow the infinite slope of the theory. To better demonstrate the agreement of the computational method with the theory, the spanwise distributions of the section-lift coefficients are also plotted in Fig. 12. The theoretical case of a wing with elliptical lift and chord distribution would have a constant section-lift coefficient across the span. Only near the wingtip do the calculated values deviate noticeably from the theory, especially in the cases with fewer spanwise panel densities.

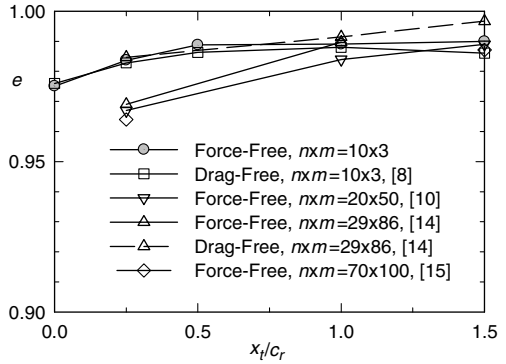

Fig. 13 Effect of tip location on the span-efficiency factor of a wing with an elliptical chord distribution at a lift coefficient of approximately 0.32; comparison of results derived with the relaxed force-free model using distributed vorticity elements and other methods of various references.

Comparison with Other Methods

The influence on the span efficiency of different planforms, all having elliptical chord distributions and lift coefficients of approximately 0.32, is shown Fig. 13. Here, the results obtained using distributed vorticity elements and a force-free wake are compared with the results of other theoretical approaches [8,10,14,15]. As discussed before, the multiple-lifting-line method of [8] uses a drag-free wake that is modeled with semi-infinite vortex sheets aligned with the freestream direction. The results of [10] were derived with a panel method that models the force-free wake using discrete potential vortices. The induced drag was computed along the trailing edge, in a manner similar to the lifting-surface method that is introduced here. The results of [14] were derived with a panel code using a force-free-wake and drag-free-wake model. The method uses higher-order panels for modeling the lifting surface and discrete vortex filaments with solid cores in the wake. Induced drag is computed in the Trefftz plane after converting the wake-vortex filaments into panels for which the doublet strengths vary piecewise linearly in the spanwise direction. The drag and lift forces of the higher-order panel code of [15] were computed using a surface-pressure integration.

Overall, the different theoretical approaches agree well over the range of investigated wingtip locations. The force-free results of the distributed vorticity element method are in good agreement with the results of the drag-free-wake models of [8,14]. Although the method introduced here agrees well with the drag-free results of [8,14] in the case of the unswept quarter-chord line ($x_t/c_r = 0.25$), small differences exist when compared with the results of the three relaxed-wake methods of [10,14,15]. Varying the panel density of the lifting surface and in the wake of the distributed vortex element method has no apparent influence on these small differences. Thus, it is assumed that the differences are inherent to the methods (for example, due to thickness effects). The method that uses distributed vorticity elements clearly requires fewer elements in the spanwise direction to achieve an accuracy that is similar to the other relaxed-wake models, thus potentially reducing the computational effort. In addition, the induced-drag computation along the trailing edge is less sensitive to changes in the panel density of the lifting surface and the wake.

Comparison with Experimental Results

One quantitative measure of the ability of the force-free potential-flow method that uses distributed vorticity element to predict the flowfield in the wake behind a wing is given in Fig. 14. The figure shows the experimental [16] and theoretical crossflow-velocity-vector fields that are located approximately two wingtip chords, or approximately 32 in., behind the trailing edge of a wind-tunnel model

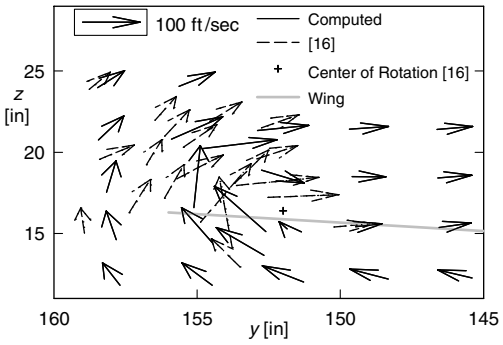

Fig. 14 Computational and experimental [16] crossflow-velocity vectors approximately two wingtip chords behind a second-generation jet-transport wing; $M_\infty = 0.700$ and $C_L = 0.53$.

of a second-generation jet-transport wing having a half-span of 156 in. As part of an investigation of the effectiveness of winglets, crossflow-velocity-vector fields were measured with a wake rake. The computational wing model consists of one row of 40 distributed vorticity elements in the spanwise direction. The planform geometry and twist are the same as those used in the experiment.

The two vector fields agree comparatively well in magnitude and direction. The major differences appear to be the locations of the centers of rotation and the location of the shear layers. The greatest differences exist near the centers of rotations for which the velocity gradients become large. Thus, small numerical errors in the computations and the influence of viscosity in the experiment are likely responsible for the deviations. To aid the comparison, the computed wake was adjusted upward by 3.5 in. in Fig. 14. Just 1.5-deg bending of the wind-tunnel model under the aerodynamic loads would explain the difference in wake offset to the rigid theoretical model. Further inaccuracies are introduced by differences in the spanwise circulation distributions as well as in the streamwise location of the crossflow surveys. Nevertheless, the agreement of the theoretical model with the experimental results, for what is a fairly difficult flowfield case, is encouraging.

Another comparison of the distributed vorticity element method with experimental results is shown in Fig. 15. In the wind-tunnel experiment, rotational speeds were measured with a vorticity meter in four transverse planes behind the 1/12-scale model of an L-19 wing [17,18]. For comparison, the computational results show contours of the crossflow velocities in the same four transverse planes that are 1, 2, 3, and 4 in. aft of the trailing edge. The root chord of the wing is 5.33 in. For the computation, the wing geometry, the freestream velocity of 110 ft/s, and the angle of attack of 12 deg are matched with the experimental values. The theoretical wing has 25 distributed vorticity elements across its half-span.

The theoretical prediction of the location of the rolled-up tip vortex agrees quite well with the experiment. The agreement with the experiment exists despite the closeness to the trailing edge of less than a chord and thus the presence of lingering viscous effects in the wake of the experiment. Those effects are indicated by the significant rotational speed contours that were measured further inboard from the wingtip. They are caused by the shear layer coming off the trailing edge that is not yet rolled up in the tip vortex. Nevertheless, the location of the shed shear layer of the experiment coincides with the location of the vortex sheet of the theoretical prediction, indicated by the dashed–dotted lines at the left of Fig. 15. Further agreement exists between the experimental and theoretical amounts of circulation that are concentrated in the rolled-up portions of the wakes. According to [17], the circulation concentrated at the tip vortices is approximately 18.4 ft^2/s in the four transverse planes. The corresponding values of the theoretical model are determined by manually computing the contour integrals along the 17.5-ft/s contour lines. The subsequent results yield circulation values of 21.8, 19.1, 26.3, and 24.5 ft^2/s in the four transverse planes that are 1, 2, 3, and 4 in. aft of the trailing edge, respectively. A more consistent agreement with the experiment is found for the 3- and 4-in. transverse planes if the integration path along the 17.5-ft/s contour line is modified along the thick dashed lines in Fig. 15. In those cases, the circulation values are 20.1 and 20.4 ft^2/s, respectively.

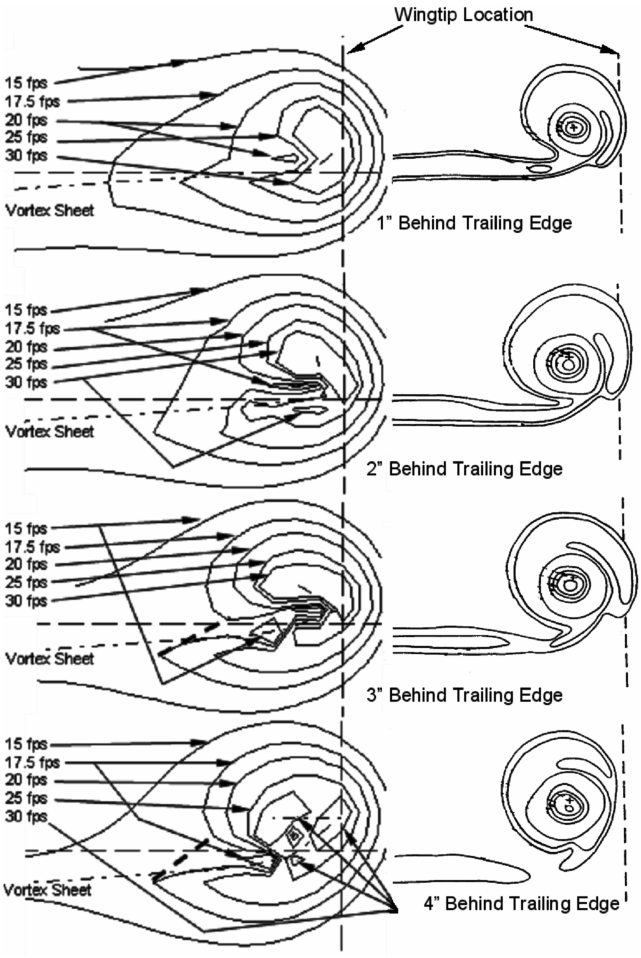

Fig. 15 Crossflow-velocity and constant rotational-speed contours in four transverse planes behind the trailing edge of a 1/12-model L-19 wing. The crossflow velocities on the left are of computational origin using distributed vorticity elements, whereas the experimental data on the right were measured with a vorticity meter [17,18].

Sample Applications

A sample application of the method that makes use of distributed vorticity elements is shown in Fig. 16. In this figure, the computed shapes of the vortex sheets are plotted as they are shed of two wings that fly in a close formation. The two wings with aspect ratios of 22 are separated by half a span in the streamwise direction and 0.8 spans in the spanwise direction. Both wings are trimmed in roll and pitch, so that their cruise-lift coefficients of 0.58 match. Although the two wake sheets intermesh strongly, the computational results are numerically well-behaved and no irregular outcomes are observed. The formation-flight configuration shown in Fig. 16 is a typical example for which the wake model has an impact on the span efficiency. In the case of the trailing wing of this particular configuration, the predicted induced drag is approximately 10% less using a fixed drag-free-wake model than with using a force-free model.

A rotating-wing example of using distributed vorticity elements is given in Fig. 17. The figure shows a rotor blade with a tip-speed ratio of five and the subsequent wake-vortex sheets of six rotations for the fixed and relaxed force-free-wake cases. The most significant differences due to the wake model are the radial expansion and axial contraction of the force-free wake, which is typical for a free-milling blade, such as is the case with a wind turbine. Clearly, the rollup behavior and the contraction/expansion of the wake have a significant impact on the velocities that are induced at the lifting

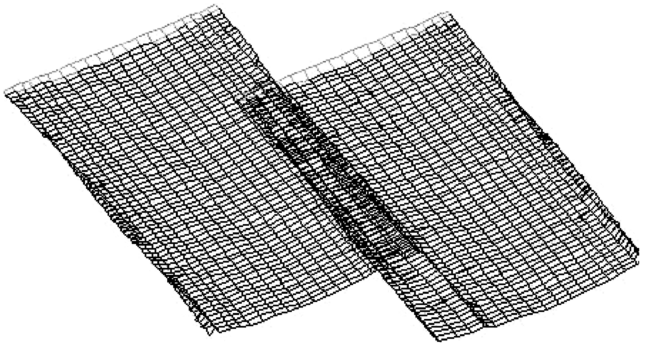

Fig. 16 Looking down at the wake-vortex sheets that are shed by wings flying in formation with a streamwise separation of $\Delta x = 0.5b$ and lateral spacing of $\Delta y = 0.8b$.

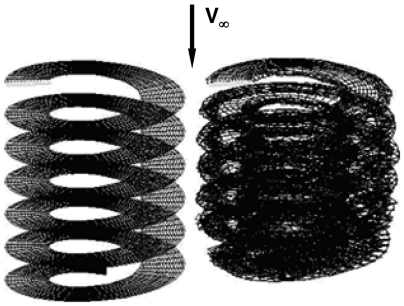

Fig. 17 A rotating wing with a tip-speed ratio of five: prescribed wake model (left) and force-free-wake model (right).

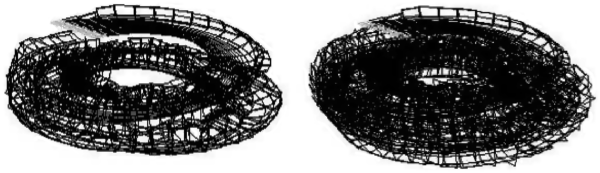

Fig. 18 A rotating wing and its wake in hover after two rotations (left) and after three rotations (right).

surface, an effect that becomes increasingly pronounced with reductions in tip-speed ratio. As far as the method is concerned, it is important to note that despite the close proximity of the wake elements of the relaxed-wake model, the solution is without any erratic behavior, even when the wake is allowed to roll up freely when the lifting surface advances.

An extreme numerical challenge is the modeling of a helicopter rotor in hover with a relaxed force-free wake. The only mechanism that transports the shed wake-vortex sheet away from the rotational plane is the self-induced-velocity field. Thus, the wake propagates downstream relatively slowly from the rotational plane, and a strong interaction occurs between the wakes shed at different blade rotations. This is clearly observed in Fig. 18, which shows a single hovering rotor blade and its subsequent wake-vortex sheet. The figure demonstrates the numerical robustness of the method, making use of distributed vorticity elements. As can be seen on the left of Fig. 18, after only a half-rotation, the shed wake already starts to merge with the wake that was shed during the previous rotation. In particular, the rolled-up tip regions of two separate rotations interact strongly and it becomes difficult to distinguish much wake structure after three rotations, as shown on the right of Fig. 18. Nevertheless, the relaxation process is well-behaved.

Conclusions

A lifting-surface method is introduced that represents the lifting surface and the vorticity that is shed into the wake using elements with distributed vorticity. In the wake, the distributed vorticity elements, because of their finite induced velocities, allow the discretized representation of a continuous vortex sheet, thus preventing the numerical issues that are typical of other relaxed-wake potential-flow methods.

The new method approach shows good agreement with the elliptically loaded wing results of the classical lifting-line theory. Likewise, good agreement exists with the results of other theoretical methods. This agreement is obtained using considerably fewer panels than the other methods considered. In particular, the drag computation along the trailing edge is less sensitive to paneling-density variations of the lifting surface and in the wake. In comparison with experimental results, the approach using distributed vorticity elements yields similar flowfields in the wake of a wing. It correctly identifies the location of the tip vortex and of the shear layer behind the wing-trailing edge. In addition to the qualitative assessments, the method well predicts the amount of circulation that is concentrated in the tip vortex and also yields very good agreement with the experiment when comparing the actual crossflow-velocity-vector fields in the wake.

The biggest advantage of using distributed vorticity elements over other potential-flow elements is their numerical robustness despite a force-free-wake model. As shown in several sample applications, the vortex-sheet rollup occurs without any erratic behavior, even when multiple wake-vortex sheets intersect each other. Overall, the numerical accuracy and stability of this method make it suitable for applications with strong interactions between the lifting surfaces and their subsequent wakes, even when the wakes need to be modeled for long distances downstream.

References

[1] Kaden, H., "Aufwicklung Einer Unstabilen Unstetigkeitsfläche," *Ingenieur-Archiv*, Vol. 2, May 1931, pp. 140–168. doi:10.1007/BF02079924

[2] Krasny, R., "Computation of Vortex Sheet Roll-Up in the Trefftz Plane," *Journal of Fluid Mechanics*, Vol. 184, 1987, pp. 123–155. doi:10.1017/S0022112087002830

[3] Rom, J., *High Angle of Attack Aerodynamics*, Springer–Verlag, New York, 1992.

[4] Portnoy, H., "Thick, Two-Dimensional Wake Roll-Up Behind a Wing of Finite Span-Extended Calculations," *Aeronautical Journal*, Vol. 81, Oct. 1977, pp. 460–463.

[5] Yeh, D. T., "Vortex Panel Calculation of Wake Rollup Behind a Large Aspect Ratio Wing," M.S. Thesis, Univ. of Maryland, College Park, MD, Apr. 1985.

[6] Nagati, M. G., Iversen, J. D., and Vogel, J. M., " Vortex Sheet Modeling with Curved Higher-Order Panels," *Journal of Aircraft*, Vol. 24, No. 11, Nov. 1987, pp. 776–782.

[7] Bramesfeld, G., "A Higher Order Vortex-Lattice Method with a Force-Free Wake," Ph.D. Dissertation, Pennsylvania State Univ., University Park, PA, Aug. 2006.

[8] Horstmann, K. H., "Ein Mehrfach-Traglinienverfahren und Seine Verwendung für Entwurf und Nachrechnung Nichtplanarer Flügelanordnungen," Ph.D. Dissertation, No. DFVLR FB 87-51, Inst. für Entwurfsaerodynamik, Braunschweig, Germany, 1987.

[9] Eppler, R., "Die Enwicklung der Tragflügeltheorie," *Ludwig-Prandtl-Gedächtnisvorlesung*, Vol. 11, Z. Flugwissenschaft, Stuttgart, Germany, Apr. 1987, pp. 133–144.

[10] Mortara, K. W., and Maughmer, M. D., "A Method for the Prediction of Induced Drag for Planar and Non-Planar Wings," AIAA Paper 93-3420, Aug. 1993.

[11] Eppler, R., and Schmidt-Göller, S., "A Method to Calculate the Influence of Vortex Roll-Up on the Induced Drag of Wings," *Finite Approximations in Fluid Mechanics 2*, DFG Priority Research Programme Results 1986-1988, Notes on Numerical Fluid Mechanics, Vol. 25, Vieweg Sohn, Braunschweig, Germany, 1989, pp. 93–107.

[12] SchmidGöller, S., "Zur Genauen Berechnung des Induzierten Widerstands von Tragflügeln," Ph.D. Dissertation, Institut a für Mechanik, Univ. Stuttgart, Stuttgart, Germnay, Oct. 1992.

[13] Munk, M. M., "Minimum Induced Drag of Aerofoils," NACA TR 121, 1921.

[14] Smith, S. C., and Kroo, I., "Computation of Induced Drag for Elliptical and Crescent-Shaped Wings," *Journal of Aircraft*, Vol. 30, No. 4, July–Aug. 1993, pp. 446–452.

[15] DeHaan, M. A., "Induced Drag of Wings with Highly Swept and Tapered Wing Tips," AIAA Paper 90-3062-CP, Aug. 1990.

[16] Flechner, S. G., Jacobs, P. F., and Whitcomb, R. T., "A High Subsonic Wing-Tunnel Investigation of Winglets on a Representative Second-Generation Jet Transport Wing," NASA TN D-8264, July 1976.

[17] Tangler, J. L., "A Study of the Vortex Sheet Immediately Behind an Aircraft Wing," M.S. Thesis, Pennsylvania State Univ., University Park, PA, 1966.

[18] McCormick, B. W., Tangler, J. L., and Sherrieb, H. E., "Structure of Trailing Vortices," *Journal of Aircraft*, Vol. 5, No. 3, May–June 1968, pp. 260–267.